Igor Goncharenko[1]
3D Incorporated,
Kanagawa-ku, Sakaecho 1-1, Urban Square,
Yokohama 221-0052, Japan
e-mail: igor@ddd.co.jp

Mikhail Svinin
Mem. ASME
e-mail: svinin@bmc.riken.jp

Shigeyuki Hosoe
e-mail: hosoe@bmc.riken.jp

Bio-Mimetic Control Research Center,
RIKEN,
Anagahora, Shimoshidami, Moriyama-ku,
Nagoya 463-0003, Japan

Dynamic Model, Haptic Solution, and Human-Inspired Motion Planning for Rolling-Based Manipulation

A virtual reality haptic system for capturing skillful human movements in control of a hemisphere rolling on a plane without slipping is presented in this paper. A dynamic model of this nonholonomic rolling system with configuration-dependent inertia and gravity is derived, and a solver, required for the real-time haptic interaction, is implemented. The performance of the haptic system is verified under experiments with human subjects. Experimental data recorded by the haptic system are analyzed and some common features of human movements in the precession phase of the manipulation of the rolling system are observed. Finally, a simple actuation scheme, capturing these features, is proposed and verified under simulation. [DOI: 10.1115/1.3074282]

1 Introduction

In recent years, there appears an interest in robotic systems where nonholonomic rolling constraints are used not only for manipulation but also for locomotion. In such systems self-propelled movements are usually generated by creating imbalance and changing the system inertia. The applications of rolling-based locomotion systems vary from the planetary surface exploration [1] to the toy industry [2]. Different designs of spherical mobile robotic systems are reported in Refs. [3–6]. These vehicles can be useful when the usage of traditional machines is limited or undesirable.

It should be noted that the analysis of motion of a sphere rolling on a plane without slipping is a classical problem in rational mechanics. The motion of a dynamically symmetric ball with a gyroscope inside (and this was perhaps the first spherical robot!) was studied in Ref. [7]. The theoretical solution obtained there was verified under experiment where the ball rolled on a plane powdered with likopodium. Note that from the viewpoint of analytical mechanics the main problem is the integrability of the motion equations in quadratures, and no notion of control is involved in the analysis. Whether or not the wealth of results obtained in analytical mechanics for rolling systems [8–10] can be utilized by control theorists and engineers yet remains to be seen.

One of the key problems in the control of nonholonomic systems with rolling constraints is the construction of motion planning algorithms. Typically, this problem is considered in the kinematic formulation [11–15], and in practical implementations the control system operates in the quasistatic mode [16–18]. The extension of the proposed motion planning algorithms to the dynamic domain is a very challenging, if not formidable, research problem. The main difficulty here is that in addition to the nonholonomic constraints one also has the configuration-dependent inertia and the gravity drift. This combination is rarely considered in the control literature, and the motion planning frameworks for such systems are not yet developed.[2]

It is also worth noting that the controllability analysis of nonholonomic systems with rolling constraints in dynamic formulation is highly nontrivial at best [19] and, in general, quite cumbersome [20]. In this situation, when the controllability analysis is not conclusive (or simply not feasible) and the controllability property needs to be hypothesized [20], the insight gained in the analysis of human movements in rolling-based manipulation and locomotion may prove helpful for attacking the motion planning problem.

It is interesting to note that trained humans and animals exhibit highly skillful movements when performing rolling-based locomotion tasks (see Fig. 1, reproducing the famous painting of Pablo Picasso "The Girl on a Ball"). Watching them performing locomotion feats on a rolling sphere in circuses, one can wonder about how these skills can be formalized in the form of a control strategy. To imitate the artistic movements, one could place a robotic mechanism on top of a spherical object. This system, however, would be extremely complex for an initial study, and it would be reasonable to resort to simplifications. In a simplified formulation, one could deal with a hemisphere and replace the robot with its center of masses projected on the main hemisphere plane. The driving principle for such a system would then be based on controlling the position of the center of mass and exploiting the nonholonomic rolling constraint to propel the hemisphere.

To extract the patterns of human movements in the control of this simplified system, one can resort to the virtual reality technology [21]. The model of a virtual hemisphere with the driving mass point is suitable for the implementation in haptic systems, because the mass point can be directly controlled by a human using a standard point-force haptic device. In a nutshell, this virtual reality haptic system would resemble the real manipulations shown in the right part of Fig. 1. Changing the position of the mass point by the haptic stylus would result into the mass redistribution and lead to the motion of the hemisphere, which can be realized in a haptic simulator. The development of such a simulator constitutes the main goal of this paper. Note that apart from discovering nontrivial motion strategies in the control of nonholonomic systems, the simulator itself can be used also for studying human motor behavior and for the development of games based on the physical modeling.

Several issues need to be addressed in the implementation of the haptic simulator. For the high fidelity force feedback, the simulation of the virtual rolling system needs to be synchronized with the haptic hardware frequency. This brings the requirement

[1]Corresponding author.

[2]To the best of our knowledge, the only exception is the study [20] where a motion planner, employing state-of-the-art algorithms of computer science (rapidly exploring random trees), is proposed.

Contributed by the Engineering Simulation and Visualization Committee of ASME for publication in the JOURNAL OF COMPUTING AND INFORMATION SCIENCE IN ENGINEERING. Manuscript received September 30, 2007; final manuscript received June 18, 2008; published online February 20, 2009. Guest Editors: J. Oliver, M. Omalley, and K. Kesavadas.

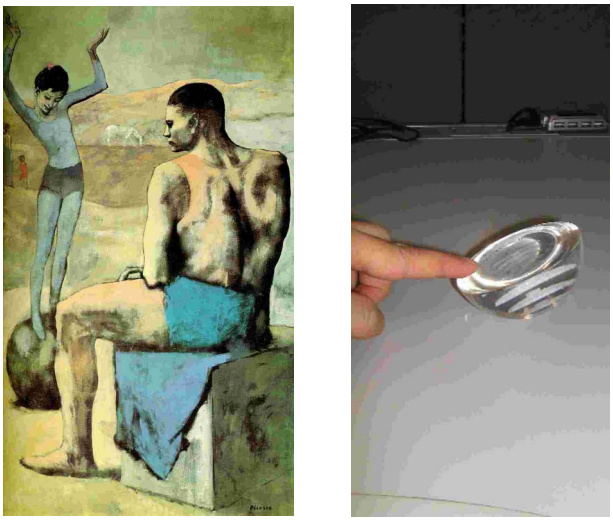

Fig. 1 Motivating example (left) and the prototype of the virtual reality haptic simulator (right)

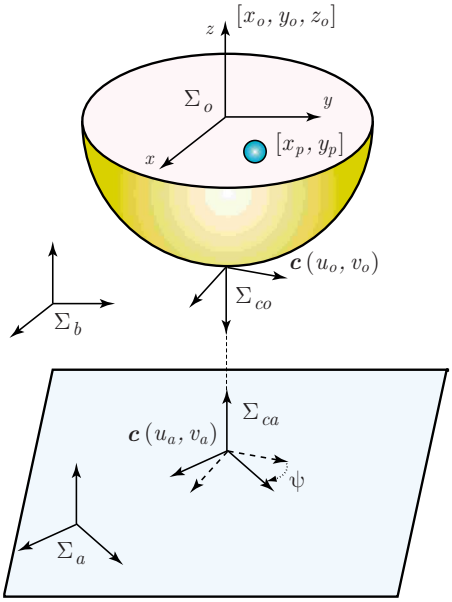

Fig. 2 System formalization

of high computational efficiency. For this purpose, the state-space dynamics of the rolling system needs to be established in the minimal form, as the often used representation employing Lagrange multipliers [6] can be more costly for real-time computations. Next, the force feedback generation procedures, suitable for the control of this system, need to be assessed, and the feasibility of the haptic rendering needs to be tested under experiments with human subjects.

The paper is organized as follows. First, in Sec. 2 we establish the kinematic and dynamic models of the rolling system under consideration. The architecture of a real-time haptic simulator is described in Sec. 3. Here, we present a solver, integrating the state dynamics, and describe force generation procedures for the haptic interaction. Initial experiments with human subjects, using the haptic simulator developed, are reported in Sec. 4. In Sec. 5, we discuss how the experimental patterns of human movements can be captured using simple mathematical models. Finally, conclusions are drawn in Sec. 6.

2 Mathematical Model

This section describes the kinematics and dynamics of a hemisphere with a mass point moving on the equatorial plane of the hemisphere. It is assumed that the hemisphere can roll on the contact plane without slipping. The effects of rolling and spinning friction are ignored.

2.1 Kinematic Model. To describe the system under consideration, we introduce the following coordinate frames (see Fig. 2): Σ_b is an inertial frame fixed at the base, Σ_o is a frame fixed at the center of the equatorial plane of the hemisphere, and Σ_a is a frame fixed at the contact plane. In addition, at the contact point we introduce the contact frame of the object Σ_{co}, and the contact frame of the plane Σ_{ca}. In what follows, we will assume that the frame Σ_a coincides with Σ_b and the frame Σ_{ca} is parallel to Σ_a.

The position of a point on the sphere is parametrized as

$$\mathbf{c}(u_o,v_o) \triangleq \mathbf{R}_y(u_o)\mathbf{R}_x(v_o)\begin{bmatrix}0\\0\\-R\end{bmatrix} = R\begin{bmatrix}-\sin u_o \cos v_o\\ \sin v_o\\ -\cos u_o \cos v_o\end{bmatrix} \tag{1}$$

where R is the radius of the sphere. The elementary rotation matrices around the axes x, y, and z are denoted by the corresponding indices. In the parametrization (1) the origin is placed at the south pole of the sphere. The geometrical meaning of the angular coordinates u_o and v_o is established as follows. The vector $\mathbf{c}(u_o,v_o)$ is obtained by rotating the vector $[0,0,-R]^T$ first around the x-axis of Σ_o through the angle v_o and then around the y-axis (of the frame associated with the first rotation) through the angle u_o. In this parametrization the lower hemisphere is selected by imposing the following constraints:

$$-\pi/2 < u_o < \pi/2, \quad -\pi/2 < v_o < \pi/2 \tag{2}$$

The parametrization ((1)) defines the Gaussian frame Σ_{co} whose orientation relative to Σ_o is

$${}^o\mathbf{R}_{co}(u_o,v_o) = \begin{bmatrix}\dfrac{\mathbf{c}_u}{|\mathbf{c}_u|} & \dfrac{\mathbf{c}_v}{|\mathbf{c}_v|} & \dfrac{\mathbf{c}_u \times \mathbf{c}_v}{|\mathbf{c}_u \times \mathbf{c}_v|}\end{bmatrix} \tag{3}$$

where $\mathbf{c}_u \triangleq \partial\mathbf{c}(u_o,v_o)/\partial u_o$ and $\mathbf{c}_v \triangleq \partial\mathbf{c}(u_o,v_o)/\partial v_o$. Having defined $\mathbf{c}_u$ and $\mathbf{c}_v$, one can write this matrix in the explicit form

$${}^o\mathbf{R}_{co}(u_o,v_o) = \begin{bmatrix}-\cos u_o & \sin u_o \sin v_o & -\sin u_o \cos v_o\\ 0 & \cos v_o & \sin v_o\\ \sin u_o & \cos u_o \sin v_o & -\cos u_o \cos v_o\end{bmatrix} \tag{4}$$

Note that this matrix can be composed of the elementary rotations as ${}^o\mathbf{R}_{co}(u_o,v_o) = \mathbf{R}_y(u_o)\mathbf{R}_x(v_o)\mathbf{R}_y(\pi)$.

Define the contact angle ψ as the angle between the x-axes of Σ_{co} and Σ_{ca} (the z-axes of these frames are aligned as depicted in Fig. 2). The orientation matrix of the sphere (the orientation of Σ_o relative to the base Σ_b) can be defined as follows. First, by superposing the axes of Σ_{co} with those of Σ_{ca}, we rotate Σ_{co} first by $\mathbf{R}_y(\pi)$ and then by $\mathbf{R}_z(\psi)$. Thus, ${}^b\mathbf{R}_{co}\mathbf{R}_y(\pi)\mathbf{R}_z(\psi) = {}^b\mathbf{R}_{ca}$ and the orientation of Σ_{ca} relative to Σ_{co} are defined as

$${}^{co}\mathbf{R}_{ca} = \mathbf{R}_y(\pi)\mathbf{R}_z(\psi) = \begin{bmatrix}-\cos\psi & \sin\psi & 0\\ \sin\psi & \cos\psi & 0\\ 0 & 0 & -1\end{bmatrix} \tag{5}$$

Then, from closing the kinematic chains associated with the coordinate frames, one obtains ${}^b\mathbf{R}_o\,{}^o\mathbf{R}_{co}\mathbf{R}_y(\pi)\mathbf{R}_z(\psi) = {}^b\mathbf{R}_{ca} \triangleq \mathbf{I}$, where $\mathbf{I}$ stands for the unit 3×3 matrix. Therefore ${}^b\mathbf{R}_o\mathbf{R}_y(u_o)\mathbf{R}_x(v_o)\mathbf{R}_z(\psi) = \mathbf{I}$ and the orientation of the sphere are defined as

$$\mathbf{R} \triangleq {}^b\mathbf{R}_o = \mathbf{R}_z^T(\psi)\mathbf{R}_x^T(v_o)\mathbf{R}_y^T(u_o) \tag{6}$$

Let $\tilde{\mathbf{v}} = [\tilde{v}_x, \tilde{v}_y, \tilde{v}_z]^T$ and $\tilde{\boldsymbol{\omega}} = [\tilde{\omega}_x, \tilde{\omega}_y, \tilde{\omega}_z]^T$ be, respectively, the translational and rotational velocities of Σ_{co} relative to Σ_{ca}. Define

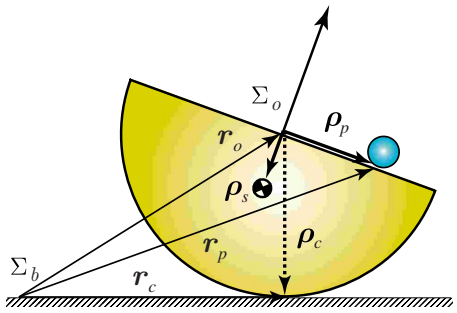

Fig. 3 Definition of basic vectors

$\mathbf{u}_{co}=[u_o,v_o]^T$ and $\mathbf{u}_{ca}=[u_a,v_a]^T$, where u_a and v_a are the coordinates of the contact point in the contact plane. The evolution of the contact coordinates is represented by the Montana equations [22,23]

$$\dot{\mathbf{u}}_{co}=\mathcal{M}_o^{-1}(\mathcal{K}_o+\tilde{\mathcal{K}}_a)^{-1}\left(\begin{bmatrix}-\tilde{\omega}_y\\ \tilde{\omega}_x\end{bmatrix}-\tilde{\mathcal{K}}_a\begin{bmatrix}\tilde{v}_x\\ \tilde{v}_y\end{bmatrix}\right) \tag{7}$$

$$\dot{\mathbf{u}}_{ca}=\mathcal{M}_a^{-1}\mathcal{R}_\psi(\mathcal{K}_o+\tilde{\mathcal{K}}_a)^{-1}\left(\begin{bmatrix}-\tilde{\omega}_y\\ \tilde{\omega}_x\end{bmatrix}+\mathcal{K}_o\begin{bmatrix}\tilde{v}_x\\ \tilde{v}_y\end{bmatrix}\right) \tag{8}$$

$$\dot{\psi}=\tilde{\omega}_z+\mathcal{T}_o\mathcal{M}_o\dot{\mathbf{u}}_{co}+\mathcal{T}_a\mathcal{M}_a\dot{\mathbf{u}}_{ca} \tag{9}$$

$$\tilde{v}_z=0 \tag{10}$$

where $\mathcal{K}_o$, $\mathcal{M}_o$, $\mathcal{T}_o$ and $\mathcal{K}_a$, $\mathcal{M}_a$, $\mathcal{T}_a$ stand for the curvature form, connection form, and the metric tensor of the surfaces o and a, respectively, at the contact point. $\mathcal{R}_\psi$ is the upper 2×2 diagonal block of the orientation matrix ((5)). $\tilde{\mathcal{K}}_a=\mathcal{R}_\psi\mathcal{K}_a\mathcal{R}_\psi$ is the curvature of a at the point of contact relative to the x- and y-axes of Σ_{co}. In our specific case, $\mathcal{M}_a=\mathbf{I}$, $\mathcal{K}_a=\mathbf{O}$, $\mathcal{T}_a=[0,0]$, and $\mathcal{M}_o=R\,\mathrm{diag}\{\cos v_o,1\}$, $\mathcal{K}_o=\mathbf{I}/R$, $\mathcal{T}_o=[\tan v_o/R,0]$. Here, $\mathbf{I}$ and $\mathbf{O}$ are, respectively, the unit and zero 2×2 matrices. Note that Eq. (10) corresponds to the holonomic constraint maintaining the contact between the bodies, while the rolling conditions are defined by the nonholonomic constraints $\tilde{v}_x=0$ and $\tilde{v}_y=0$.

Let $\boldsymbol{\omega}_o=\{\omega_x,\omega_y,\omega_z\}^T$ be the angular velocity of the frame Σ_o, defined in projections onto the axis of the base frame Σ_b. The vectors $\boldsymbol{\omega}$ and $\tilde{\boldsymbol{\omega}}$ are related as $\tilde{\boldsymbol{\omega}}={}^{co}\mathbf{R}_{ca}\boldsymbol{\omega}_o$. Expressing the contact kinematic equations (7)–(9) in terms of the components of $\boldsymbol{\omega}_o$, one obtains

$$\dot{u}_a=R\omega_y \tag{11}$$

$$\dot{v}_a=-R\omega_x \tag{12}$$

$$\dot{u}_o=-(\omega_x\sin\psi+\omega_y\cos\psi)/\cos v_o \tag{13}$$

$$\dot{v}_o=-\omega_x\cos\psi+\omega_y\sin\psi \tag{14}$$

$$\dot{\psi}=-\omega_z-(\omega_x\sin\psi+\omega_y\cos\psi)\tan v_o \tag{15}$$

Note that we do not impose the so-called no-spinning constraint ($\omega_z=0$) because it is difficult to justify its validity in our actuation scheme.

2.2 Dynamic Model. Let $\mathbf{r}_o$ be the vector of the origin of the frame Σ_o, $\mathbf{v}_o$ its absolute velocity, and $\boldsymbol{\omega}_o$ is the angular velocity of the frame Σ_o. The unit base vectors of the frame Σ_o are denoted by $\mathbf{i}_o,\mathbf{j}_o,\mathbf{k}_o$, and those of the inertial frame Σ_b are denoted by $\mathbf{i}_b$, $\mathbf{j}_b$, and $\mathbf{k}_b$. The system under consideration is propelled by moving the mass point P and thus changing the system inertia and the gravity center (see Fig. 3). The absolute position of the mass point is denoted by the vector $\mathbf{r}_p$, and its absolute velocity by the vector $\mathbf{v}_p$. The position of the mass point with respect to the origin of Σ_o is denoted by $\boldsymbol{\rho}_p$.

It is assumed that the particle moves on the main hemisphere plane, and the vector of the driving force $\mathbf{F}$ acting on the point mass lies in the main hemisphere plane. Therefore, the relative position $\boldsymbol{\rho}_p$ and the driving force $\mathbf{F}$ can be parametrized as $\boldsymbol{\rho}_p\triangleq\mathbf{i}_o x_p+\mathbf{j}_o y_p=\mathbf{RNp}$, $\mathbf{F}\triangleq\mathbf{i}_o f_x+\mathbf{j}_o f_y=\mathbf{RNf}$, where $\mathbf{p}\triangleq\{x_p,y_p\}^T$, $\mathbf{f}\triangleq\{f_x,f_y\}^T$, $\mathbf{R}$ is the matrix of orientation of the frame Σ_o with respect to Σ_b, and the projection matrix

$$\mathbf{N}\triangleq\begin{bmatrix}1&0\\0&1\\0&0\end{bmatrix} \tag{16}$$

This matrix is necessary to keep the z-components of the projections of the vectors $\boldsymbol{\rho}_p$ and $\mathbf{F}$ onto the axes of the frame Σ_o zero.

The derivation of the dynamic model will be based on the use of D'Alembert's principle [24]. Let $\delta\mathbf{r}_o$ and $\delta\mathbf{r}_p$ be the virtual displacements of the origin of Σ_o and the driving point, respectively, and $\delta\boldsymbol{\pi}_o$ be the vector of infinitesimal rotation of Σ_o. For the unconstrained system composed of the hemisphere and the point mass, D'Alembert's principle can be written down as follows:

$$\begin{aligned}&\delta\mathbf{r}_o\cdot\{m_s\dot{\mathbf{v}}_o+\dot{\boldsymbol{\omega}}_o\times m_s\boldsymbol{\rho}_s+\boldsymbol{\omega}_o\times(\boldsymbol{\omega}_o\times m_s\boldsymbol{\rho}_s)-m_s\mathbf{g}\}\\&\quad+\delta\boldsymbol{\pi}_o\cdot\{m_s\boldsymbol{\rho}_s\times\dot{\mathbf{v}}_o+\mathbf{J}_o\dot{\boldsymbol{\omega}}_o+\boldsymbol{\omega}_o\times\mathbf{J}_o\boldsymbol{\omega}_o-\boldsymbol{\rho}_s\times m_s\mathbf{g}\}\\&\quad+\delta\mathbf{r}_p\cdot\{m_p\dot{\mathbf{v}}_p-m_p\mathbf{g}-\mathbf{F}\}=0\end{aligned} \tag{17}$$

where m_s is the mass of the hemisphere, m_p is the mass of the particle, $\boldsymbol{\rho}_s$ is the vector of the center of mass of the hemisphere defined in the frame Σ_o, $\mathbf{J}_o$ is the inertia tensor of the hemisphere with respect to the origin of Σ_o, and $\mathbf{g}$ is the gravity vector. Under the assumption that the hemisphere is homogeneous, $\boldsymbol{\rho}_s=-\frac{3}{8}R\,\mathbf{k}_o$, $\mathbf{J}_o=\frac{2}{5}m_sR^2\mathbf{I}$, where $\mathbf{I}$ stands for the unit tensor.

First, we need to transform $\delta\mathbf{r}_p$ in Eq. (17) to $\delta\mathbf{r}_o$, $\delta\boldsymbol{\pi}_o$, and $\delta'\boldsymbol{\rho}_p$, where $\delta'\boldsymbol{\rho}_p\triangleq\mathbf{i}_o\delta x_p+\mathbf{j}_o\delta y_p=\mathbf{RN}\delta\mathbf{p}$ is the virtual displacement of the driving point relative to Σ_o. Taking into account that $\mathbf{r}_p=\mathbf{r}_o+\boldsymbol{\rho}_p$, $\delta\mathbf{r}_p=\delta\mathbf{r}_o+\delta\boldsymbol{\pi}_o\times\boldsymbol{\rho}_p+\delta'\boldsymbol{\rho}_p$, and $\boldsymbol{\omega}_o\times\mathbf{J}_o\boldsymbol{\omega}_o=0$, we transform Eq. (17) to the following form:

$$\begin{aligned}&\delta\mathbf{r}_o\cdot\{m_s\dot{\mathbf{v}}_o+\dot{\boldsymbol{\omega}}_o\times m_s\boldsymbol{\rho}_s+\boldsymbol{\omega}_o\times(\boldsymbol{\omega}_o\times m_s\boldsymbol{\rho}_s)+m_p\dot{\mathbf{v}}_p\\&\quad-(m_s+m_p)\mathbf{g}-\mathbf{F}\}+\delta\boldsymbol{\pi}_o\cdot\{m_s\boldsymbol{\rho}_s\times\dot{\mathbf{v}}_o+\mathbf{J}_o\dot{\boldsymbol{\omega}}_o\\&\quad+\boldsymbol{\rho}_p\times m_p\dot{\mathbf{v}}_p-(m_s\boldsymbol{\rho}_s+m_p\boldsymbol{\rho}_p)\times\mathbf{g}-\boldsymbol{\rho}_p\times\mathbf{F}\}\\&\quad+\delta'\boldsymbol{\rho}_p\cdot\{m_p\dot{\mathbf{v}}_p-m_p\mathbf{g}-\mathbf{F}\}=0\end{aligned} \tag{18}$$

Here, the terms involving $\mathbf{v}_p$ and $\dot{\mathbf{v}}_p$ can be expanded further by the kinematic formulas $\mathbf{v}_p=\mathbf{v}_o+\boldsymbol{\omega}_o\times\boldsymbol{\rho}_p+\mathring{\boldsymbol{\rho}}_p$ and $\dot{\mathbf{v}}_p=\dot{\mathbf{v}}_o+\dot{\boldsymbol{\omega}}_o\times\boldsymbol{\rho}_p+\boldsymbol{\omega}_o\times(\boldsymbol{\omega}_o\times\boldsymbol{\rho}_p)+2\boldsymbol{\omega}_o\times\mathring{\boldsymbol{\rho}}_p+\mathring{\mathring{\boldsymbol{\rho}}}_p$, where the local derivatives are defined as $\mathring{\boldsymbol{\rho}}_p\triangleq\mathbf{i}_o\dot{x}_p+\mathbf{j}_o\dot{y}_p=\mathbf{RN}\dot{\mathbf{p}}$ and $\mathring{\mathring{\boldsymbol{\rho}}}_p\triangleq\mathbf{i}_o\ddot{x}_p+\mathbf{j}_o\ddot{y}_p=\mathbf{RN}\ddot{\mathbf{p}}$.

Next, we transform the virtual displacement $\delta\mathbf{r}_o$ in Eq. (18) to the point of contact, defined by the vector $\mathbf{r}_c$ (see Fig. 3). The reason is to introduce variations in quasicoordinates that would vanish by virtue of the nonholonomic constraints [25]. Taking into account that $\mathbf{r}_c=\mathbf{r}_o+\boldsymbol{\rho}_c$, $\delta\mathbf{r}_c=\delta\mathbf{r}_o+\delta\boldsymbol{\pi}_o\times\boldsymbol{\rho}_c$, and $\boldsymbol{\rho}_c\times\mathbf{g}=0$, where $\boldsymbol{\rho}_c=-R\,\mathbf{k}_b$, we transform Eq. (18) to the following form:

$$\begin{aligned}&\delta\mathbf{r}_c\cdot\{m_s\dot{\mathbf{v}}_o+\dot{\boldsymbol{\omega}}_o\times m_s\boldsymbol{\rho}_s+\boldsymbol{\omega}_o\times(\boldsymbol{\omega}_o\times m_s\boldsymbol{\rho}_s)+m_p\dot{\mathbf{v}}_p\\&\quad-(m_s+m_p)\mathbf{g}-\mathbf{F}\}+\delta\boldsymbol{\pi}_o\cdot\{m_s(\boldsymbol{\rho}_s-\boldsymbol{\rho}_c)\times\dot{\mathbf{v}}_o\\&\quad+\mathbf{J}_o\dot{\boldsymbol{\omega}}_o-\boldsymbol{\rho}_c\times[\dot{\boldsymbol{\omega}}_o\times m_s\boldsymbol{\rho}_s+\boldsymbol{\omega}_o\times(\boldsymbol{\omega}_o\times m_s\boldsymbol{\rho}_s)]\\&\quad+(\boldsymbol{\rho}_p-\boldsymbol{\rho}_c)\times m_p\dot{\mathbf{v}}_p-(m_s\boldsymbol{\rho}_s+m_p\boldsymbol{\rho}_p)\times\mathbf{g}\\&\quad-(\boldsymbol{\rho}_p-\boldsymbol{\rho}_c)\times\mathbf{F}\}+\delta'\boldsymbol{\rho}_p\cdot\{m_p\dot{\mathbf{v}}_p-m_p\mathbf{g}-\mathbf{F}\}=0.\end{aligned} \tag{19}$$

The rolling constraints, formulated in terms of the variations in

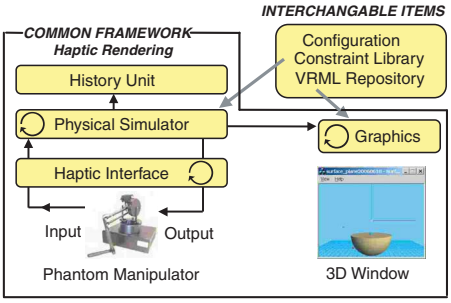

Fig. 4 System architecture

the quasicoordinates, can be written down as $\delta \mathbf{r}_c = 0$, and the corresponding terms in Eq. (19) do not enter the dynamic equations (the standard procedure based on the introduction of the Lagrangian multipliers moves the terms in the corresponding brackets to the constraint reactions [26]).

In deriving the motion equations from Eq. (19) we can eliminate the terms with $\dot{\mathbf{v}}_o$ using the fact that $\mathbf{v}_o + \boldsymbol{\omega}_o \times \boldsymbol{\rho}_c = 0$, and, therefore, $\dot{\mathbf{v}}_o = -\dot{\boldsymbol{\omega}}_o \times \boldsymbol{\rho}_c$. Now, setting δx_p, δy_p and $\delta \boldsymbol{\pi}_o$ as the independent variations, we obtain from Eq. (19) the dynamic equations for the mass point

$$\mathbf{N}^T \mathbf{R}^T \{ m_p \dot{\mathbf{v}}_p - m_p \mathbf{g} \} = \mathbf{f} \tag{20}$$

and for the hemisphere

$$\mathbf{J}_c \dot{\boldsymbol{\omega}}_o - \boldsymbol{\rho}_c \times [\boldsymbol{\omega}_o \times (\boldsymbol{\omega}_o \times m_s \boldsymbol{\rho}_s)] + (\boldsymbol{\rho}_p - \boldsymbol{\rho}_c) \times m_p \dot{\mathbf{v}}_p - (m_s \boldsymbol{\rho}_s + m_p \boldsymbol{\rho}_p) \times \mathbf{g} - (\boldsymbol{\rho}_p - \boldsymbol{\rho}_c) \times \mathbf{F} = 0 \tag{21}$$

where $\mathbf{J}_c = \mathbf{J}_o + m_s(\hat{\boldsymbol{\rho}}_s \hat{\boldsymbol{\rho}}_c + \hat{\boldsymbol{\rho}}_c \hat{\boldsymbol{\rho}}_s - \hat{\boldsymbol{\rho}}_c \hat{\boldsymbol{\rho}}_c)$ is the inertia tensor of the hemisphere at the contact point, and hat is the skew-symmetric operator such that $\mathbf{a} \times \mathbf{a} \equiv \hat{\mathbf{a}} \mathbf{a}$.

3 Design and Implementation of the Haptic Simulator

To record and analyze human movements in the manipulation of the hemisphere rolling on the plane, we built a virtual reality haptic system. The system architecture is schematically shown in Fig. 4. The hardware part of the system is based on a point-force haptic device (PHANToM Premium 1.5 manipulator, 3DOF, maximum exertable force 8.5 N) connected to a PC (dual core CPU, Intel Pentium 4, 3.0 GHz) through a PCI (Peripheral Component Interconnect) interface.

The software runs in two threads responsible for independent haptic and graphical renderings. In the haptic rendering loop, the *Physical Simulator* module integrates the system of first-order ordinary differential equations (ODEs), describing the evolution of the rolling system under a specified force input in the time domain. The state dynamics are simulated in real time (using fourth-order Runge–Kutta method [27] with constant step $h = 0.001$ s) and the haptic feedback is supplied to the human hand through the PHANToM stylus. Thus, the simulation is synchronized with the constant haptic hardware frequency (1000 Hz).

Similar to the architecture presented in Ref. [28], the ODE solver and the haptic feedback generation procedures are dynamically linked to the library of external constraints. When the application starts, the Physical Simulator module acquires in real time the position and velocity of the PHANToM stylus, calculates the haptic feedback force and the force applied to the virtual reality object, and integrates the ODEs to obtain the state of the system at the next moment of time. The geometric output of this module, the position and orientation of the hemisphere with the mass point, is rendered in the *3D Window* by the graphical thread.

The *History Unit* module records all the time histories of the state variables as well as the haptic feedback forces. These data are recorded at 100 Hz, which is enough to analyze human movements in our manipulation task. The physical parameters of the

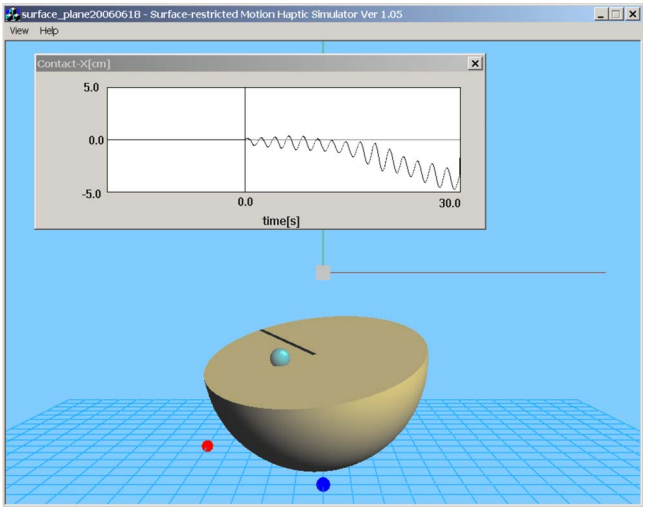

Fig. 5 Graphical user interface

rolling system as well as the initial and the target values of the state variables are defined in the *Configuration* module. The graphical representation of the rolling system (referred to as a Virtual Reality Modeling Language (VRML) scene) is also defined in this module. Different segments (files) of the VRML scene are collected in the configuration repository. The VRML files define the geometry of the hemisphere and the mass point drawn as a small sphere on the main hemisphere plane.

The initial position of the rolling system is shown in Fig. 4. The graphical user interface, shown in Fig. 5, corresponds to the state of the rolling system after 30 s of haptic interaction. In this figure, the real-time scrolling window displays the evolution of the x-coordinate of the contact trajectory.

The rest of this section describes in detail the structure of the ODE solver and the haptic feedback force models in our simulator.

3.1 Solver. The state of the system under consideration (rolling hemisphere with moving mass point) can be described in terms of 12 variables. The 12-dimensional state vector

$$\mathbf{x} = \{ \mathbf{p}^T, \dot{\mathbf{p}}^T, \boldsymbol{\omega}_o^T, \mathbf{u}_{ca}^T, \mathbf{u}_{co}^T, \psi \}^T \tag{22}$$

or $\mathbf{x} = \{x_p, y_p, \dot{x}_p, \dot{y}_p, \omega_x, \omega_y, \omega_z, u_a, v_a, u_o, v_o, \psi\}^T$ in the expanded form. The solver integrates the system of differential equations $\dot{\mathbf{x}} = \mathbf{X}(\mathbf{x}, \mathbf{f})$, describing the evolution of the state vector $\mathbf{x}$ under the input force $\mathbf{f}$. To form the right-hand part $\mathbf{X}(\mathbf{x}, \mathbf{f})$ of the state dynamics, we first need to define $\ddot{\mathbf{p}}$ and $\dot{\boldsymbol{\omega}}_o$ as functions of $\mathbf{x}$ and $\mathbf{f}$. Upon expressing $\dot{\mathbf{v}}_p$ in Eqs. (20) and (21) through the state variables, one can represent the dynamic equations (20) and (21) in the following matrix form:

$$\begin{bmatrix} \mathbf{H}_{pp} & \mathbf{H}_{ps} \\ \mathbf{H}_{sp} & \mathbf{H}_{ss} \end{bmatrix} \begin{bmatrix} \ddot{\mathbf{p}} \\ \dot{\boldsymbol{\omega}}_o \end{bmatrix} = \begin{bmatrix} \mathbf{h}_p \\ \mathbf{h}_s \end{bmatrix} \tag{23}$$

where

$$\mathbf{H}_{pp} = m_p \mathbf{I} \tag{24}$$

$$\mathbf{H}_{ps} = -m_p \mathbf{N}^T \mathbf{R}^T \widehat{(\boldsymbol{\rho}_p - \boldsymbol{\rho}_c)} \tag{25}$$

$$\mathbf{H}_{sp} = m_p \widehat{(\boldsymbol{\rho}_p - \boldsymbol{\rho}_c)} \mathbf{R} \mathbf{N} = \mathbf{H}_{ps}^T \tag{26}$$

$$\mathbf{H}_{ss} = \mathbf{J}_c - m_p \widehat{(\boldsymbol{\rho}_p - \boldsymbol{\rho}_c)}^2 \tag{27}$$

$$\mathbf{h}_p = \mathbf{f} - m_p \mathbf{N}^T \mathbf{R}^T [\boldsymbol{\omega}_o \times (\boldsymbol{\omega}_o \times \boldsymbol{\rho}_p) + 2\boldsymbol{\omega}_o \times \mathring{\boldsymbol{\rho}}_p - \mathbf{g}] \tag{28}$$

$$\mathbf{h}_s = (\boldsymbol{\rho}_p - \boldsymbol{\rho}_c) \times \mathbf{RNf} - m_p(\boldsymbol{\rho}_p - \boldsymbol{\rho}_c) \times [\boldsymbol{\omega}_o \times (\boldsymbol{\omega}_o \times \boldsymbol{\rho}_p) + 2\boldsymbol{\omega}_o \times \mathring{\boldsymbol{\rho}}_p] + \boldsymbol{\rho}_c \times [\boldsymbol{\omega}_o \times (\boldsymbol{\omega}_o \times m_s\boldsymbol{\rho}_s)] + (m_s\boldsymbol{\rho}_s + m_p\boldsymbol{\rho}_p) \times \mathbf{g} \tag{29}$$

Having formed the system matrices, one can define the accelerations

$$\begin{bmatrix} \ddot{\mathbf{p}} \\ \dot{\boldsymbol{\omega}}_o \end{bmatrix} = \begin{bmatrix} \mathbf{H}_{pp} & \mathbf{H}_{ps} \\ \mathbf{H}_{sp} & \mathbf{H}_{ss} \end{bmatrix}^{-1} \begin{bmatrix} \mathbf{h}_p \\ \mathbf{h}_s \end{bmatrix} \triangleq \begin{bmatrix} \mathcal{P}(\mathbf{x},\mathbf{f}) \\ \mathcal{Q}(\mathbf{x},\mathbf{f}) \end{bmatrix} \tag{30}$$

and then compile the kinematic and dynamic equations (11)–(15) and (30) into the state-space form

$$\dot{\mathbf{x}} \triangleq \begin{bmatrix} \dot{\mathbf{p}} \\ \ddot{\mathbf{p}} \\ \dot{\boldsymbol{\omega}}_o \\ \dot{u}_a \\ \dot{v}_a \\ \dot{u}_o \\ \dot{v}_o \\ \dot{\psi} \end{bmatrix} = \begin{bmatrix} \dot{\mathbf{p}} \\ \mathcal{P}(\mathbf{x},\mathbf{f}) \\ \mathcal{Q}(\mathbf{x},\mathbf{f}) \\ R\omega_y \\ -R\omega_x \\ -(\omega_x \sin\psi + \omega_y \cos\psi)/\cos v_o \\ -\omega_x \cos\psi + \omega_y \sin\psi \\ -\omega_z - (\omega_x \sin\psi + \omega_y \cos\psi)\tan v_o \end{bmatrix} \triangleq \mathbf{X}(\mathbf{x},\mathbf{f}) \tag{31}$$

To be able to simulate the state dynamics ((31)) in real time, the numerical integration of the state equations must be synchronized with the constant haptic hardware frequency (1000 Hz). This constitutes higher requirements to the efficiency of the computation of the right-hand part of the state equations ((31)). To increase the computational efficiency, one can reduce the inversion of the 5×5 system matrix in Eq. (30) to the inversion of a 3×3 matrix. Let us define

$$\begin{bmatrix} \mathbf{H}_{pp} & \mathbf{H}_{ps} \\ \mathbf{H}_{sp} & \mathbf{H}_{ss} \end{bmatrix}^{-1} \triangleq \begin{bmatrix} \mathcal{H}_{pp} & \mathcal{H}_{ps} \\ \mathcal{H}_{sp} & \mathcal{H}_{ss} \end{bmatrix} \tag{32}$$

where, in the general case, the blocks if the inverse matrix are defined as [29]

$$\mathcal{H}_{ss} = (\mathbf{H}_{ss} - \mathbf{H}_{sp}\mathbf{H}_{pp}^{-1}\mathbf{H}_{ps})^{-1} \tag{33}$$

$$\mathcal{H}_{ps} = -\mathbf{H}_{pp}^{-1}\mathbf{H}_{ps}\mathcal{H}_{ss} \tag{34}$$

$$\mathcal{H}_{sp} = -\mathcal{H}_{ss}\mathbf{H}_{sp}\mathbf{H}_{pp}^{-1} \tag{35}$$

$$\mathcal{H}_{pp} = \mathbf{H}_{pp}^{-1} + \mathbf{H}_{pp}^{-1}\mathbf{H}_{ps}\mathcal{H}_{ss}\mathbf{H}_{sp}\mathbf{H}_{pp}^{-1} \tag{36}$$

The straight computation of the matrix blocks for the system under consideration leads to the following formulas:

$$\mathcal{H}_{ss} = (\mathbf{J}_c + m_p\widehat{(\boldsymbol{\rho}_p - \boldsymbol{\rho}_c)}\mathbf{k}_o\mathbf{k}_o^T\widehat{(\boldsymbol{\rho}_p - \boldsymbol{\rho}_c)}^T)^{-1} \tag{37}$$

$$\mathcal{H}_{ps} = -\mathbf{N}^T\mathbf{R}^T\widehat{(\boldsymbol{\rho}_p - \boldsymbol{\rho}_c)}^T\mathcal{H}_{ss} \tag{38}$$

$$\mathcal{H}_{sp} = -\mathcal{H}_{ss}\widehat{(\boldsymbol{\rho}_p - \boldsymbol{\rho}_c)}\mathbf{RN} = \mathcal{H}_{ps}^T \tag{39}$$

$$\mathcal{H}_{pp} = \frac{1}{m_p}\mathbf{I} + \mathbf{N}^T\mathbf{R}^T\widehat{(\boldsymbol{\rho}_p - \boldsymbol{\rho}_c)}^T\mathcal{H}_{ss}\widehat{(\boldsymbol{\rho}_p - \boldsymbol{\rho}_c)}\mathbf{RN} \tag{40}$$

Thus, in the calculation of the matrix ((32)) we need to inverse only the 3×3 matrix in Eq. (37). Note that this inverse matrix is never singular (unless the mass of the sphere $m_s = 0$). Also note that in the software coding the last term ((40)) can be computed as $\mathcal{H}_{pp} = (1/m_p)\mathbf{I} + \mathcal{H}_{ps}\mathcal{H}_{ss}^{-1}\mathcal{H}_{sp}$.

3.2 Force Input. The input force $\mathbf{f}$, driving the point mass in the dynamic model, is to be defined from the force $\mathbf{F}_h$ developed at the human hand through the haptic interface. Typically, in the impedance-type haptic devices the force $\mathbf{F}_h$ is defined using virtual spring-damper models [30]. These models generate the haptic force $\mathbf{F}_h$ based on the position and velocity differences between the haptic proxy (the end-point of the PHANToM manipulator transformed to the virtual space) and a virtual object (the driven mass point, in our case). The haptic force is generated in real time and is supplied to the hardware interface.

Note that in programming the PHANToM manipulator the haptic force $\mathbf{F}_h$ is specified in the inertial (base) frame [31]. Let $\mathbf{r}_h$ and $\mathbf{v}_h$ be, respectively, the absolute position and velocity of the haptic point. The absolute position and velocity of the particle are defined as $\mathbf{r}_p = \mathbf{r}_o + \boldsymbol{\rho}_p$, and $\mathbf{v}_p = \boldsymbol{\omega}_o \times (\boldsymbol{\rho}_p - \boldsymbol{\rho}_c) + \mathring{\boldsymbol{\rho}}_p$, where coordinates of the center of the sphere are $\mathbf{r}_o = \{u_a, v_a, R\}^T$, and $\boldsymbol{\rho}_p = \mathbf{RNp}$, $\mathring{\boldsymbol{\rho}}_p = \mathbf{RN}\dot{\mathbf{p}}$. Having defined these quantities, one can calculate the haptic force in the inertial frame. The following three solutions are implemented in our haptic simulator.

First method (M1). The haptic interaction between the human hand and the mass point is modeled by the elastic force with the spring and damping matrices proportional to the unit matrix

$$\mathbf{F}_h = -k_r(\mathbf{r}_p - \mathbf{r}_h) - k_v(\mathbf{v}_p - \mathbf{v}_h) \tag{41}$$

where k_r and k_v are the scalar stiffness and damping coefficients. To define the driving force $\mathbf{f}$, one needs to transform $\mathbf{F}_h$ into the moving frame Σ_o, and then project it onto the main hemisphere plain. As a result, one obtains

$$\mathbf{f} = \mathbf{N}^T\mathbf{R}^T\mathbf{F}_h \tag{42}$$

This method has one disadvantage. When the haptic force $\mathbf{F}_h$ is orthogonal to the main hemisphere plane it does not affect the motion equation. This may produce some unrealistic feeling for the user.

Second method (M2). This method is a simple modification of the first one. As before, we define the haptic force by Eq. (41). Then, we replace $\mathbf{f}$ in Eq. (28) with $\mathbf{N}^T\mathbf{R}^T\mathbf{F}_h$, and in Eq. (29) we replace the term $\mathbf{RNf}$ with $\mathbf{F}_h$. From the perceptional point of view this model can be more realistic. In this model, when the haptic force $\mathbf{F}_h$ is orthogonal to the main hemisphere plane it does not affect the motion of the particle but it does affect the motion of the hemisphere.

Third method (M3). This method is similar to the second one but the haptic force here is defined differently

$$\mathbf{F}_h = -\mathbf{K}_r(\mathbf{r}_p - \mathbf{r}_h) - \mathbf{K}_v(\mathbf{v}_p - \mathbf{v}_h) \tag{43}$$

where $\mathbf{K}_r$ and $\mathbf{K}_v$ are the stiffness and damping matrices expressed in the inertial (base) frame. How do we specify them? Consider first the stiffness matrix. When there is no damping, Eq. (43) can be written as $\mathbf{F}_h^{(b)} = -\mathbf{K}_r^{(b)}\Delta\mathbf{r}^{(b)}$. Here, by the upper superscript we denote the frame (the base Σ_b or the object Σ_o) in which a vector or tensor quantity is expressed. Since $\mathbf{F}_h^{(b)} = \mathbf{RF}_h^{(o)}$ and $\Delta\mathbf{r}^{(b)} = \mathbf{R}\Delta\mathbf{r}^{(o)}$, we get $\mathbf{F}_h^{(o)} = -\mathbf{R}^T\mathbf{K}_r^{(b)}\mathbf{R}\Delta\mathbf{r}^{(o)} \triangleq -\mathbf{K}_r^{(o)}\Delta\mathbf{r}^{(o)}$, and therefore

$$\mathbf{K}_r \triangleq \mathbf{K}_r^{(b)} = \mathbf{RK}_r^{(o)}\mathbf{R}^T \tag{44}$$

Here, the stiffness matrix in the object frame can be specified as $\mathbf{K}_r^{(o)} = \mathrm{diag}\{k_{rx}, k_{ry}, k_{rz}\}$, where $k_{rx} = k_{ry}$ and $k_{rz} \gg k_{rx}$. If the coefficients are specified in this way, the user will feel the "plane constraint." It will be harder to move the particle perpendicular to the main hemisphere plane compared with the "in-plane" movements. Thus, this method of modeling the haptic interaction can be more realistic.

The damping matrix in Eq. (43) is defined in the similar way. Specifically, we assign

$$\mathbf{K}_v \triangleq \mathbf{K}_v^{(b)} = \mathbf{RK}_v^{(o)}\mathbf{R}^T \tag{45}$$

where the damping matrix in the object frame is $\mathbf{K}_v^{(o)} = \mathrm{diag}\{k_{vx}, k_{vy}, k_{vz}\}$, and $k_{vx} = k_{vy}$ and $k_{vz} \gg k_{vx}$.

It is instructive to clarify the differences among the three methods from the standpoint of perception. In the first method, when the haptic force $\mathbf{F}_h$ does not lie in the main hemisphere plane, its

out-of-plane component does not enter the motion equations. When it happens, the user may feel strange sensations, resulting from mismatching of the visual and haptic information and leading to unrealistic perception of the system behavior. This situation is excluded in the second and third methods, as we allow for the out-of-plane component of $\mathbf{F}_h$ to influence the motion of the rolling system. Thus, these methods are expected to produce more realistic perception of the system behavior.

The difference between the second and third methods is only in the specification of the stiffness and damping tensors. Specifically, in the second method these tensors are isotropic (given by Eq. (41)) while in the third method they can be anisotropic (defined by Eq. (43)). Setting the coefficients of the anisotropic tensors in a right way can allow the user to feel the main hemisphere plane as the out-of-plane movement of the haptic proxy would be felt with greater resistance. The idea of the anisotropic tensors is basically similar to that of the compliance control of robotic mechanisms in constrained movements [32]. In principle, the third method can produce more realistic perception. However, the design of the stable haptic interaction in this method becomes complex and requires special techniques [33,34].

4 Experiments

The experimental system, described in Sec. 3, was used for analysis of human movements in the manipulation of the virtual rolling system. In the experiments, the parameters of the system were configured as follows. The gravity acceleration and the masses of the driving point and the hemisphere were set to 9.81 $\mathrm{m/s^2}$, 1 kg, and 0.1 kg, respectively. The radius of the hemisphere was set as $R=4$ cm.

Four naïve subjects (males, aged between 25 and 30 years old, three right-handed and one left-handed) participated in the experiments. The subjects were instructed to transport the hemisphere from the initial configuration, where all the state variables (Eq. (22)) are zero, to a final state and stop it there. At the initial configuration the system was at rest, with the main symmetry axis of the hemisphere vertical and the point mass being on the top of the hemisphere, as shown in the 3*D Window* block of Fig. 4. Before starting the movement the subject positioned the haptic proxy at the point mass and switched on the haptic interaction by pressing a button on the computer keyboard.

In the target configuration the vector $\mathbf{u}_{ca}$ was set as $\{-4, -4\}^T$ cm while the vectors $\mathbf{p}$, $\dot{\mathbf{p}}$, $\boldsymbol{\omega}$, and $\mathbf{u}_{co}$ were set zero. The component ψ of the state vector $\mathbf{x}$ at the target configuration was not specified.[3] Geometrically, this means that at the target configuration the system is at rest, the main symmetry axis of the hemisphere is vertical, the balancing point mass is on the top of the hemisphere, but the orientation of the hemisphere, defined at this state only by the angle ψ, can be arbitrary.

The subjects were requested to produce the reaching movements in a natural way, on their own pace, trading off the speed and the comfortability. A movement trial was considered to be successful if the movement task was completed within 4 min and within certain position and velocity tolerances. The subject was given an audio feedback, generated by the computer, if a trial was successful. In the course of preliminary evaluations, the following tolerances were specified: $\Delta\omega = \pm 0.01$ rad/s for the components of the angular velocity of the hemisphere, $\Delta u_{ca} = \pm 0.4$ cm for the components of the contact point on the plane, $\Delta u_{co} = \pm \pi/18$ rad for the components of the contact point on the hemisphere, $\Delta p = \pm 0.4$ cm and $\Delta \dot{p} = \pm 0.4$ cm/s for the components of, respectively, the position and velocity of the driving mass point.

[3]In the preliminary evaluations, we found that specifying the complete orientation at the target configuration made the reaching task much more complex. One can speculate that the acquisition of the necessary motor skills for such a task requires considerably more learning time.

4.1 Assessment of the Force Feedback Methods. The experiments with the human subjects were conducted in two days. On the first day we conducted a general evaluation of the subject performance. The subjects familiarized with the experimental setup, comprehended the reaching task, and performed movement trials. During these preliminary experiments we also conducted the assessment of the force feedback methods described in Sec. 3.2.

For the methods M1 and M2, the PHANToM stiffness and damping coefficients were set as, respectively, $k_r = 250$ N/m and $k_v = 10$ N s/m. It was found that when using the method M1, all the subjects could manipulate the rolling system and transport it to the target configuration. However, they mentioned strange sensations and inconveniences in the manipulation of the hemisphere when the hand movement was in the direction orthogonal to the equatorial plane. Compare with the method M1, the subjects found the method M2 easier and more comfortable.

In assessing method M3, we set $k_{rx} = k_{ry} = 250$ N/m, $k_{vx} = k_{vy} = 10$ N s/m, and varied the ratio $\alpha = k_{rz}/k_{rx} = k_{vz}/k_{vx}$ from 1 to 4. When the ratio factor α was closed to or exceeded 4, the subjects evaluated the control as bumpy, uncomfortable, and unstable. While the exact stability analysis is out of the scope of this paper, the subjects' perceptions can be partially explained by the apparatus limitations—the PHANToM manufacturer [7] does not recommend setting up the stiffness coefficients more than 800 Nm.

In the course of the experiments, it was found that when the ratio factor α varied from 1.5 to 2.5, the control of the hemisphere was stable, with smooth force sensations. As a result, the subjects manipulated the rolling system faster; two subjects could complete the reaching task within 40 s time interval several times. Overall, among the three methods for the generation of the feedback force, the subjects preferred method M3 (with $\alpha = 2$) as more natural, comfortable, and realistic in perception. They sensed better the object reaction force and the inertial properties of the system.

Finally, it should be mentioned that in the assessment of the force feedback methods we also experimented with a special case when the driving force $\mathbf{f}$, sent to the physical simulator, was calculated correctly but the haptic force $\mathbf{F}_h$ was zeroed when applied to the hand through the PHANToM stylus. This corresponds to the visual-based control without the haptic perception. In this case all the subjects failed to produce the requested reaching movements. Even though the subjects could see that the point mass followed the hand movement, they could not control the system as the hemisphere motion became quite chaotic. They reasoned that the system became uncontrollable without the haptic feedback. This fact may evidence that the central nervous system cannot control constrained movements based only on visual information.

4.2 Experimental Results. On the second day of the experiments, the subjects performed 15 movement trials, using method M3 with $\alpha = 2$, and the data were collected for analysis. In all the trials the movement task was completed successfully. However, the movement time was varied from 46 s to 170 s.

It is interesting to note that the subjects showed roughly similar motion patterns resulting possibly from a similar control strategy. When asked, after the experiments, about their perceptions, the subjects reported they felt loosing control of the system if they visually concentrated on the position of the point mass and/or that of the haptic proxy. It appears that they paid visual attention mostly to the current and target contact points on the contact plane while controlling the motion of the hemisphere through the haptic feedback.

When asked about their movements, the subjects could not identify the specific trajectory of the hand. However, the general movement strategy, reconstructed from their comments, can be summarized as follows. First, they tried to slightly unbalance the hemisphere and then gently increase its precession. Having developed a certain level of the hemisphere precession, they tried to

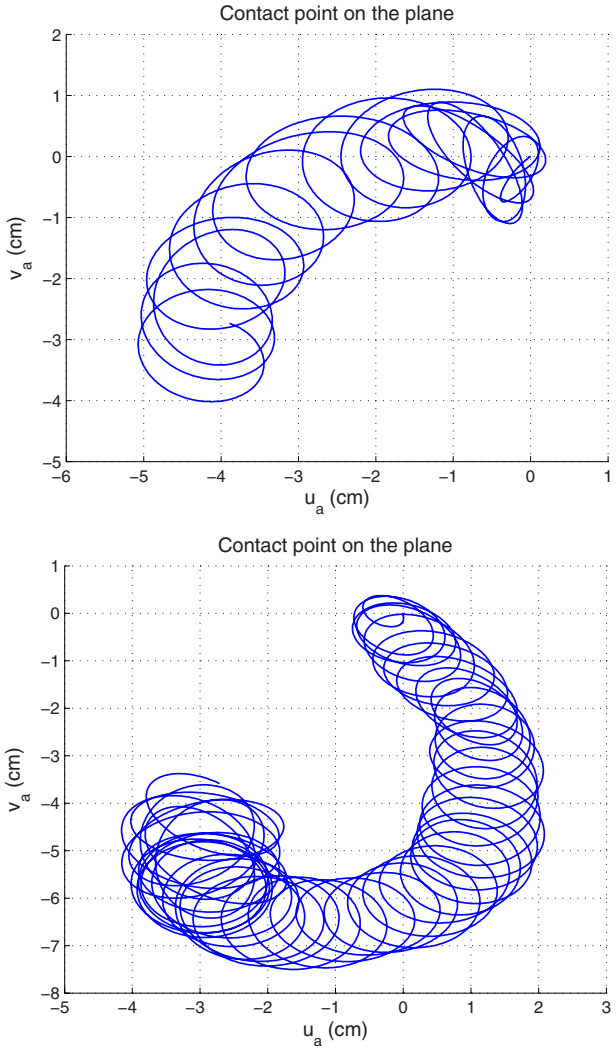

Fig. 6 Contact point trajectories for the right-handed (top) and left-handed (bottom) subjects

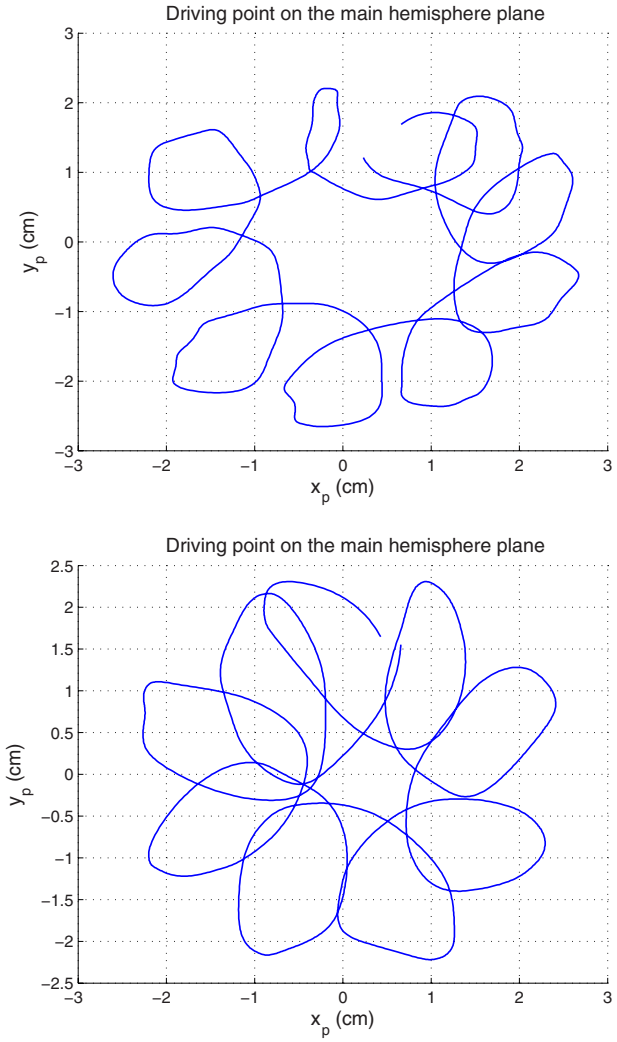

Fig. 7 Driving point trajectories for the right-handed (top) and left-handed (bottom) subjects

keep it constant until the rolling system reached a vicinity of the target point at the contact plane. At the final stage of the maneuver, the subjects decreased the precession and tried to stabilize the angular movements of the hemisphere. This was produced by somewhat jerky, if not chaotic, movements of the hand. All the subjects mentioned that the choice of the precession axis and the precession speed is important for the successful steering of the rolling system

There can be two reasons why all the subjects preferred this strategy. First, it appears to be conceptually simple and, therefore, it could be more comfortable. The second reason is not physical or physiological but rather social. The subjects could observe the trials of the current performer and discuss them between each other. So, once a successful motion strategy was picked by someone it could be reproduced by the others.

Two examples of the trajectory of the contact point in the contact plane are shown in Fig. 6. The trajectories are circularly curved and appear to be helical. The corresponding trajectories of the driving point mass in the equatorial plane of the hemisphere are shown in Fig. 7. To keep the graphs clean and readable, these trajectories are taken for 20 s intervals of time in the middle part of the movement depicted in Fig. 6. The trace of the curves in Fig. 7 is almost closed, and the curves themselves appear to be roselike. One may conjecture that one leaf of the rose corresponds to one spiral loop in Fig. 6. This roselike pattern was visible in all the subjects' data. The number of leaves varied from 8 or 15 (on average 10). The leaf radius changed from 0.4 cm to 1.0 cm (on average 0.7 cm), while the outer radius of the roselike curve varied from 1.2 cm to 2.4 cm (on average 1.8 cm). Also, the time span featuring the roselike pattern varied from 18 s to 32 s (on average 23 s).

5 Simple Actuation Scheme

Having observed the pattern of human movements, reported in Sec. 4, we would like to explain its formation using, as much as possible, simple mathematical tools. In general, the hand trajectory is composed of the acceleration, the steady state precession, and the deceleration/stabilization phases. In what follows, we will be interested in capturing only the precession phase of this trajectory.

Assume for simplicity that the human can perfectly control and specify the trajectory $\mathbf{p}(t)$ of the mass point on the main hemisphere plane. From first equation in Eq. (23) we get

$$\mathbf{H}_{pp}\ddot{\mathbf{p}} + \mathbf{H}_{ps}\dot{\boldsymbol{\omega}}_o = \mathbf{f} + \hat{\mathbf{h}}_p \tag{46}$$

where $\hat{\mathbf{h}}_p \triangleq (\mathbf{h}_p)_{\mathbf{f}=0}$ is defined by Eq. (28) with $\mathbf{f}=0$. Let also $\hat{\mathbf{h}}_s \triangleq (\mathbf{h}_s)_{\mathbf{f}=0}$. It is defined by Eq. (29) with $\mathbf{f}=0$. Upon substituting Eq. (46) into Eq, (23), after some algebra one obtains

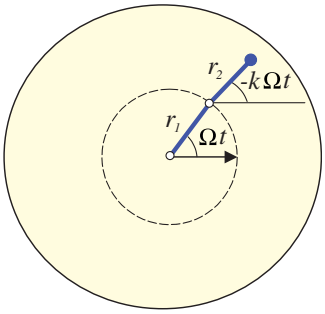

Fig. 8 Double pendulum as a propelling mechanism

$$\dot{\boldsymbol{\omega}}_o = (\mathbf{H}_{ss} - \widehat{(\boldsymbol{\rho}_p - \boldsymbol{\rho}_c)}\mathbf{R}\mathbf{N}\mathbf{H}_{ps})^{-1}(\hat{\mathbf{h}}_s - \widehat{(\boldsymbol{\rho}_p - \boldsymbol{\rho}_c)}\mathbf{R}\mathbf{N}\hat{\mathbf{h}}_p) \quad (47)$$

Note that under our assumption (the direct specification of $\mathbf{p}$) the acceleration of the mass point $\ddot{\mathbf{p}}$ does not influence the angular acceleration of the sphere as it does not enter the sphere dynamics ((47)).

The dynamics of the system under consideration can be described now in terms of eight state variables. The eight-dimensional state vector $\mathbf{x}=\{\boldsymbol{\omega}_o^T, \mathbf{u}_{ca}^T, \mathbf{u}_{co}^T, \psi\}^T$, or, in the expanded form $\mathbf{x}=\{\omega_x, \omega_y, \omega_z, u_a, v_a, u_o, v_o, \psi\}^T$. Since the trajectory of the mass point is specified explicitly as a function of time, the state dynamics $\dot{\mathbf{x}}=\mathbf{X}(\mathbf{x}, \mathbf{p}(t), \dot{\mathbf{p}}(t))$ are defined as

$$\underbrace{\begin{bmatrix} \dot{\boldsymbol{\omega}}_o \\ \dot{u}_a \\ \dot{v}_a \\ \dot{u}_o \\ \dot{v}_o \\ \dot{\psi} \end{bmatrix}}_{\dot{\mathbf{x}}} = \underbrace{\begin{bmatrix} \hat{\mathcal{Q}}(\mathbf{x}, \mathbf{p}(t), \dot{\mathbf{p}}(t)) \\ R\omega_y \\ -R\omega_x \\ -(\omega_x \sin\psi + \omega_y \cos\psi)/\cos v_o \\ -\omega_x \cos\psi + \omega_y \sin\psi \\ -\omega_z - (\omega_x \sin\psi + \omega_y \cos\psi)\tan v_o \end{bmatrix}}_{\mathbf{X}(\mathbf{x}, \mathbf{p}(t), \dot{\mathbf{p}}(t))} \quad (48)$$

where $\hat{\mathcal{Q}}$ is defined by the right-hand side of Eq. (47). By integrating the state dynamics ((48)), one first finds the system evolution $\mathbf{x}(t)$ and then estimates from Eq. (46) the driving force $\mathbf{f}(t)$ corresponding to the prescribed motion of the particle $\mathbf{p}(t)$.

To qualitatively capture the pattern of human movements, shown in Fig. 7, one may look for a family of roselike curves with an adjustable number of leaves. There are many such curves known in the literature [35]. In our study, we model the trajectory $\mathbf{p}(t)$ of the mass point as

$$x_p(t) = r_1 \cos\varphi(t) + r_2 \cos(k\,\varphi(t)) \quad (49)$$

$$y_p(t) = r_1 \sin\varphi(t) - r_2 \sin(k\,\varphi(t)) \quad (50)$$

This curve describes the trajectory of the end-point of a virtual double pendulum with the link lengths r_1 and r_2, rotating in the equatorial plane of the hemisphere, as shown in Fig. 8. The links of the pendulum are rotated in the opposite directions, with the first link circulating $k+1$ times slower than the second one. If the parameter k is integer the curve is closed and it has $k+1$ leaves. To capture the precession phase of the human trajectory, one specifies the motion of the joint angle as $\varphi(t)=\Omega t$, where Ω is a constant parameter.

Note that the curve (Eqs. (49) and (50)) can be viewed as a partial case of epitrochoids. However, the double pendulum interpretation is more attractive. One can think of the double pendulum as a propeller, and it gives a mechanical analog for our actuation scheme.

The idea of the double pendulum actuation scheme can be supported by a simulation example. In the example, in accordance

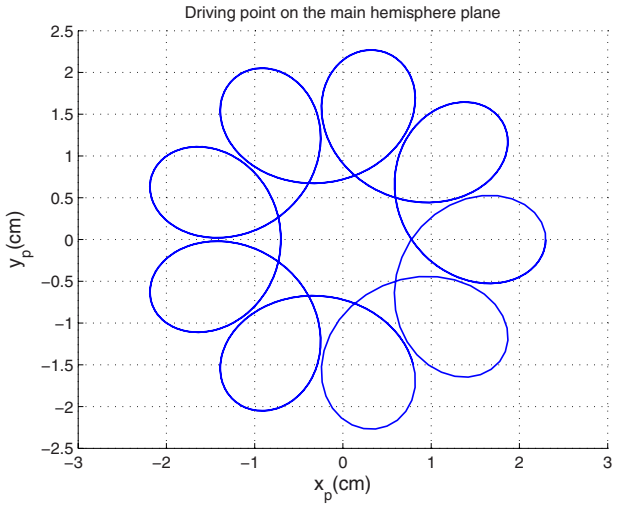

Fig. 9 Roselike trajectory of the mass point on the equatorial plane

with the experimental data reported in Sec. 4, we set $r_1=1.5$ cm and $r_2=0.8$ cm. To obtain one closed cycle with nine leaves we set $k=8$. The precession constant is set as $\Omega=-\pi/10$ rad/s, which corresponds to the clockwise rotation of the first link and counterclockwise rotation of the second link. The position of the driving mass point in the equatorial plane of the hemisphere, defined by the curve (Eqs. (49) and (50)), is shown in Fig. 9. As can be seen, qualitatively, the roselike pattern of human movements is captured.

Having specified $\mathbf{p}(t)$, we then integrated the state dynamic equations ((48)). The motion is simulated on the time interval [0, 35] s. Note that the initial position of the mass point is not zero, and in the simulation we start to move the hemisphere from the equilibrium state corresponding to $\mathbf{p}(0)$. This can be considered as a modeling uncertainty. Figure 10 shows the trajectory of the contact point on the contact plane. The trajectory resembles that shown in Fig. 6 (top). As can be seen, qualitatively, the basic features of this trajectory (the curvature of the trace and the spiral-like loops along the trace) are similar to those observed in the human movements.

While the comparison conducted may look optimistic and speaks in favor of the actuation scheme given by Eqs. (49) and (50), the real story of human manipulations is, most probably, still

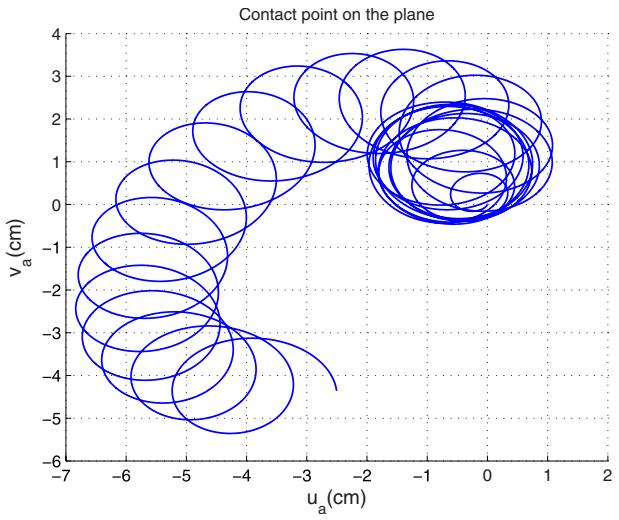

Fig. 10 Trajectory of the contact point in the contact plane

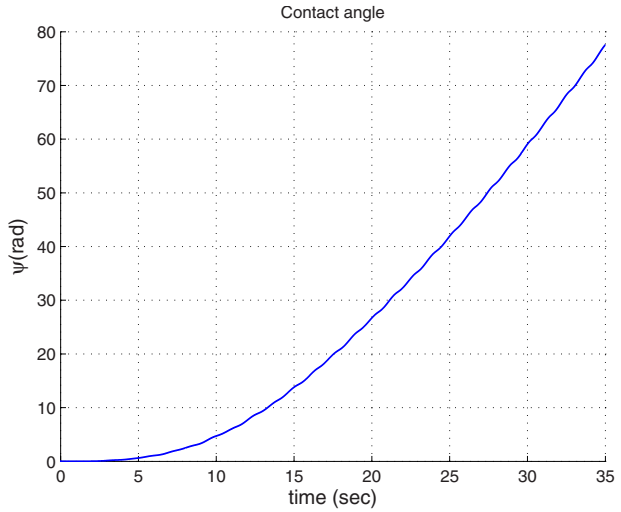

Fig. 11 Precession angle ψ

far from being that simple. In this connection, it should be noted that in the course of simulation we found the motion of the hemisphere to be very sensitive to the choice of k, Ω, r_1, and r_2. We also found that the curvature of the arc trace observed in the experimental data is achieved only for a relatively narrow range of these parameters. In this range the precession speed becomes almost constant (see Fig. 11) after recovering from initial imbalance caused by the nonzero values of $\mathbf{p}(0)$. The exact tuning of these parameters (or their possible self-synchronization in the course of the production of comfortable periodic movements) remains an open issue.

Note that the proposed mechanism for capturing the pattern of human movements is applicable only for the middle part of the trajectory. It does not work for the beginning (acceleration phase) and end (deceleration/stabilization) parts where the patterns of the hand movements are quite different. In principle, the actuation scheme given by Eqs. (49) and (50) can form a part of a motion planner for the generation of humanlike movements for rolling-based locomotion and manipulation systems. However, it captures only the general tendency of the rhythmic movement in the precession phase. Different mechanisms for the generation of such movements can be realized using the approaches developed in biological cybernetics. In particular, it is believed that in the central nervous system the generation of complex periodic movements is organized in the form of a central pattern generator [36] that, computationally, can be implemented by a network of coupled oscillators [37]. Testing this approach for the generation of humanlike movements in control of nonholonomic systems with rolling constraints would be an interesting subject for future research.

6 Conclusions

A virtual reality haptic system for capturing skillful human movements in control of a hemisphere rolling on a plane without slipping has been presented in this paper. To steer the hemisphere, a mass point, moving in the main hemisphere plane and changing the system inertia and the gravity center, was introduced. The driving principle for the rolling system is based on controlling the position of the mass point by the human hand via a haptic device. A dynamic model of the nonholonomic rolling system with configuration-dependent inertia and gravity has been derived, and a solver, required for the real-time haptic interaction, has been implemented.

The performance of the haptic system has been verified under experiments with human subjects. It was confirmed that the control of the rolling system is very hard, if not impossible, without the kinesthetic sensations provided by the feedback forces. When estimating the haptic feedback, the subjects preferred the one that provides the better feeling of the reaction from the main hemisphere plane. Experimental data recorded by the haptic system were analyzed and some common features of the human movement in the manipulation of the rolling system have been observed. In particular, it was found that the trajectory of the contact point in the contact plane appears to be helical, with its path being circularly curved. At the same time the trajectory of the driving mass point looks like a periodic rose curve. A simple actuation scheme, capturing this pattern of human movements, has been proposed and verified under simulation.

As we see it now, the haptic simulator presented in this paper can be used mainly for discovering nontrivial motion strategies in the control of nonholonomic systems with rolling constraints, as the analytical motion planning techniques for such systems are very hard to construct. Apart from the main purpose, we believe the simulator developed can be used also for studying human motor behavior and in gaming applications based on the physical modeling.

Several issues should be addressed in future research. First, it would be reasonable to include in our model the effects of rolling and spinning frictions ignored in the current study. Next, a rigorous analysis of the stability of the haptic interaction would be necessary for the finer tuning of the feedback force models with anisotropic stiffness and damping. Finally, it would be interesting to analyze the formation of the human trajectory not only in the middle (precession phase) part but also in the acceleration and deceleration phases. The prediction of the whole trajectory is, perhaps, an ambitious goal, but is worth trying.

Acknowledgment

The authors would like thank the anonymous referees for helpful comments and valuable suggestions.

References

[1] Michaud, F., de Lafontaine, J., and Caron, S., 2001, "A Spherical Robot for Planetary Surface Exploration," *Proceedings of the Sixth International Symposium on Artificial Intelligence, Robotics and Automation in Space*, Canadian Space Agency, St-Hubert Quebec, Canada.
[2] Michaud, F., and Caron, S., 2002, "Roball, the Rolling Robot," Auton. Rob., **12**(2), pp. 211–222.
[3] Bicchi, A., Balluchi, A., Prattichizzo, D., and Gorelli, A., 1997, "Introducing the 'Sphericle': An Experimental Testbed for Research and Teaching in Nonholonomy," *Proceedings of the IEEE International Conference on Robotics and Automation*, Vol. 3, pp. 2620–2625.
[4] Bhattacharya, S., and Agrawal, S., 2000, "Spherical Rolling Robot: A Design and Motion Planning Studies," IEEE Trans. Rob. Autom., **16**(6), pp. 835–839.
[5] Javadi A., A. H., and Mojabi, P., 2004, "Introducing Glory: A Novel Strategy for an Omnidirectional Spherical Rolling Robot," ASME J. Dyn. Syst., Meas., Control, **126**(3), pp. 678–683.
[6] Balasubramanian, R., 2006, "Modeling and Control Techniques for a Class of Mobile Robot Error Recovery Problems," Ph.D. thesis, Carnegie Mellon University, Pittsburgh, PA.
[7] Bobylev, D., 1892, "On a Ball With a Gyroscope Inside Rolling Without Sliding on a Horizontal Plane," Mat. Sb., **16**(3), pp. 544–581.
[8] Chaplygin, S., 1949, "On a Ball Rolling on the Horizontal Plane," *Investigations on the Dynamics of Nonholonomic Systems* (Classics of Natural Science), N. Semenova, ed., GITTL, Moscow, pp. 72–99, in Russian.
[9] Kilin, A., 2001, "The Dynamics of Chaplygin Ball: The Qualitative and Computer Analysis," Regular Chaotic Dyn., **6**(3), pp. 291–306.
[10] Borisov, A., and Mamaev, I., 2002, "Rolling of a Rigid Body on Plane and Sphere: Hierarchy of Dynamics," Regular Chaotic Dyn., **7**(2), pp. 177–200.
[11] Li, Z., and Canny, J., 1990, "Motion of Two Rigid Bodies With Rolling Constraint," IEEE Trans. Rob. Autom., **6**(1), pp. 62–72.
[12] Jurdjevic, V., 1993, "The Geometry of the Plate-Ball Problem," Arch. Ration. Mech. Anal., **124**(4), pp. 305–328.
[13] Marigo, A., and Bicchi, A., 2000, "Rolling Bodies With Regular Surface: Controllability Theory and Applications," IEEE Trans. Autom. Control, **45**(9), pp. 1586–1599.
[14] Mukherjee, R., Minor, M., and Pukrushpan, J., 2002, "Motion Planning for a Spherical Mobile Robot: Revisiting the Classical Ball-Plate Problem," ASME J. Dyn. Syst., Meas., Control, **124**(4), pp. 502–511.
[15] Svinin, M., and Hosoe, S., 2008, "Motion Planning Algorithms for a Rolling Sphere With Limited Contact Area," IEEE Transactions on Robotics, **24**(3), pp. 612–625.
[16] Camicia, C., Conticelli, F., and Bicchi, A., 2000, "Nonholonomic Kinematics

and Dynamics of the Spherical," *Proceedings of the IEEE/RSJ International Conference on Intelligent Robots and Systems, IROS'2000*, pp. 805–810.
[17] Harada, K., Kawashima, T., and Kaneko, M., 2002, "Rolling Based Manipulation Under Neighborhood Equilibrium," Int. J. Robot. Res., **21**(5–6), pp. 463–474.
[18] Suzuki, K., Svinin, M., and Hosoe, S., 2005, "Motion Planning for Rolling Based Locomotion," Journal of Robotics and Mechatronics, **17**(5), pp. 537–545.
[19] Hristu-Varsakelis, D., 2001, "The Dynamics of a Forced Sphere-Plate Mechanical System," IEEE Trans. Autom. Control, **46**(5), pp. 678–686.
[20] Choudhury, P., and Lynch, K., 2002, "Rolling Manipulation With a Single Control," Int. J. Robot. Res., **21**(5–6), pp. 475–487.
[21] Burdea, G., 2003, *Virtual Reality Technology*, 2nd ed., Wiley, New York.
[22] Montana, D., 1988, "The Kinematics of Contact and Grasp," Int. J. Robot. Res., **7**(3), pp. 17–32.
[23] Murray, R., Li, Z., and Sastry, S., 1994, *A Mathematical Introduction to Robotic Manipulation*, CRC, Boca Raton, FL.
[24] Wittenburg, J., 1977, *Dynamics of Systems of Rigid Bodies*, Teubner, Stuttgart, Germany.
[25] Neimark, J., and Fufaev, N., 1972, "Dynamics of Nonholonomic Systems," *Translation of Mathematical Monographs*, Vol. 33, American Mathematical Society, Providence, RI.
[26] Lurie, A., 2002, "Analytical Mechanics," *Foundations of Engineering Mechanics*. Springer-Verlag, Berlin.
[27] Press, W., Teukolsky, S., Vetterling, W., and Flannery, B., 1992, *Numerical Recipes in C: The Art of Scientific Computing*, Cambridge University Press, New York.
[28] Goncharenko, I., Svinin, M., Kanou, Y., and Hosoe, S., 2006, "Predictability of Rest-to-Rest Movements in Haptic Environments With 3D Constraints," Journal of Robotics and Mechatronics, **18**(4), pp. 458–466.
[29] Horn, R., and Johnson, C., 1986, *Matrix Analysis*, Cambridge University Press, Cambridge.
[30] Burdea, G., 1996, *Force and Touch Feedback for Virtual Reality*, Wiley, New York.
[31] SensAble Devices Inc., PHANToM Master User's Manual, http://sensable.com.
[32] Craig, J., 1989, *Introduction to Robotics: Mechanics and Control*, 2nd ed., Addison-Wesley, Reading, MA.
[33] Hogan, N., and Colgate, J., 1989, "Stability Problems in Contact Tasks," *Robotics Review*, Vol. 1, J. Craig, O. Khatib, and T. Lozano-Perez, eds., MIT, Cambridge, MA, pp. 339–348.
[34] Miller, B., Colgate, J., and Freeman, R., 2000, "Guaranteed Stability of Haptic Systems With Nonlinear Virtual Environments," IEEE Trans. Rob. Autom., **16**(6), pp. 712–719.
[35] Gray, A., 1998, *Modern Differential Geometry of Curves and Surfaces With Mathematica*, 2nd ed., CRC, Boca Raton, FL.
[36] Marder, E., and Calabrese, R., 1996, "Principles of Rhythmic Motor Pattern Generation," Physiol. Rev., **76**, pp. 688–717.
[37] Matsuoka, K., 1987, "Mechanisms of Frequency and Pattern Control in the Neural Rhythm Generators," Biol. Cybern., **56**, pp. 345–353.